



Reprogrammable 3D Mesostructures Through Compressive Buckling of Thin Films with Prestrained Shape Memory Polymer

Xiaogang Guo¹ Zheng Xu² Fan Zhang¹ Xueju Wang³ Yanyang Zi²
John A. Rogers⁴ Yonggang Huang⁵ Yihui Zhang^{1*}

⁽¹⁾Department of Engineering Mechanics, Center for Mechanics and Materials and Center for Flexible Electronics Technology, AML, Tsinghua University, Beijing 100084, China)

⁽²⁾State Key Laboratory for Manufacturing and Systems Engineering, School of Mechanical Engineering, Xi'an Jiaotong University, Xi'an 710049, China)

⁽³⁾Simpson Querrey Institute and Feinberg Medical School, Center for Bio-Integrated Electronics, Northwestern University, Evanston, IL 60208, USA)

⁽⁴⁾Departments of Materials Science and Engineering, Biomedical Engineering, Chemistry, Mechanical Engineering, Electrical Engineering and Computer Science, and Neurological Surgery, Center for Bio-Integrated Electronics, Simpson Querrey Institute for Nano/biotechnology Northwestern University, Evanston, IL 60208, USA)

⁽⁵⁾Departments of Civil and Environmental Engineering, Mechanical Engineering, and Materials Science and Engineering, Center for Bio-Integrated Electronics, Northwestern University, Evanston, IL 60208, USA)

Received 18 July 2018; revision received 23 July 2018; Accepted 24 July 2018;
published online 9 August 2018

© The Chinese Society of Theoretical and Applied Mechanics 2018

ABSTRACT The mechanically guided assembly that relies on the compressive buckling of strategically patterned 2D thin films represents a robust route to complex 3D mesostructures in advanced materials and even functional micro-devices. Based on this approach, formation of complex 3D configurations with suspended curvy features or hierarchical geometries remains a challenge. In this paper, we incorporate the prestrained shape memory polymer in the 2D precursor design to enable local rolling deformations after the mechanical assembly through compressive buckling. A theoretical model captures quantitatively the effect of key design parameters on local rolling deformations. The combination of precisely controlled global buckling and local rolling expands substantially the range of accessible 3D configurations. The combined experimental and theoretical studies over a dozen of examples demonstrate the utility of the proposed strategy in achieving complex reprogrammable 3D mesostructures.

KEY WORDS Mechanically guided 3D assembly, Reprogrammable 3D mesostructures, Shape memory polymer, Buckling, Rolling

1. Introduction

Manufacture of complex 3D mesostructures in advanced materials with different feature sizes is an area of rapidly increasing interest, due to their promising applications in areas of energy storage [1–8], metamaterial [9–11], biomedical devices [12–16], and electronics [17–26]. Many different approaches,

* Corresponding author. E-mail: yihuizhang@tsinghua.edu.cn

for example 3D printing [5, 16, 27–37], controlled folding [14, 38–43], and template growth [44–47], were developed for the assembly of complex 3D mesostructures. Most of the existing approaches are constrained by the accessible range of material types or 3D geometries [48, 49]. In particular, it is very challenging to exploit these approaches to form complex 3D electronic devices consisting of high-performance materials (e.g., single-crystal semiconductors). Recently, a mechanically guided approach that relies on the compressive buckling of strategically patterned 2D thin films has been developed to achieve deterministic assembly of complex 3D mesostructures and functional devices [48, 50–53]. Aside from the applicability to a broad set of materials, this approach also applies over different length scales, with feature sizes ranging from hundreds of nanometers to tens of centimeters. Despite the recent progress, the formation of complex 3D configurations with suspended curvy features remains a challenge based on the mechanically guided assembly. Additionally, significant opportunities also remain in the development of this assembly approach to achieve reprogrammable 3D mesostructures.

In this manuscript, we incorporate a prestrained shape memory polymer (SMP) layer into the laminated 2D precursor structure, which can be used to achieve a temperature-controlled local actuation, subsequent to the compressive buckling, thereby reshaping the mechanically assembled 3D mesostructures. The degree of local actuation, mainly in the form of rolling, can be well controlled by the level of prestrain in the SMP and the thickness ratio between the actuation layer and the supporting layer, as illustrated by both the mechanics modeling and the experiments. The combination of global buckling and local rolling enables the formation of curvy features at desired regions of the assembled mesostructures, thereby substantially extending the accessible range of 3D configurations. Quantitative agreements between the experimental and computational results suggest the mechanics modeling as a reliable tool to achieve a diversity of reprogrammable 3D mesostructures, through the strategic selections of 2D precursor layouts, location of prestrained SMP layer, bonding conditions, and even heating paths.

2. Fabrication and Modeling of a Laminated SMP for Controlled Rolling

Figure 1a illustrates the fabrication procedure of laminated shape memory polymer that undergoes rolling deformations upon heating. The fabrication began with printing an SMP layer (Veroblue, a typical UV cured SMP material) using the PolyJet 3D printing technique (Object 260VS, Stratasys). Stretching the printed Veroblue layer at a high temperature ($> T_g$, the glass transition temperature $\sim 63^\circ\text{C}$), followed by a cooling process while fixing the applied strain, generates a prestrained Veroblue layer to serve as the actuation layer. Casting a thin layer of Veroblue solution on the top surface of another printed supporting layer (also in Veroblue, $60\ \mu\text{m}$ in thickness) enables a strong bonding between the actuation and supporting layers after curing using the ultraviolet (UV) light for a few minutes. During the UV curing, pressing the laminated structure with a small pressure (30 kPa) squeezes the extra solution out, thereby ensuring a relative uniform adhesion layer ($30\ \mu\text{m}$ in thickness). Heating the laminated SMP structure above the glass transition temperature triggers the strain release in the actuation layer, resulting in a uniform rolling deformation, as shown in Fig. 1a.

Figure 1b presents a set of experimental results that illustrate the rolling deformations in laminated SMP structure formed using the above method. Here, the structure was immersed into hot water (100°C) to trigger its rolling deformation that completes very quickly (e.g., within a second). Since all of the different (actuation, adhesion, and supporting) layers are made of Veroblue in the current fabrication method, the laminated SMP structure has very robust interfaces, as evidenced by the rightmost experimental image (Fig. 1b). Here, no delamination was observed as the structure underwent a very large rolling deformation. In particular, the cured adhesion layer is essentially composed of the same material as the supporting layer, with both acting as the passive layer during the thermally activated deformation. As such, the laminated SMP ribbon structure can be modeled as a bilayer beam (length L) consisting of an actuation layer (thickness t_a and prestrain ε_{pre}) and a passive layer (thickness t_p and no prestrain), as shown in Fig. 1c. It is then easy to understand that the degree of rolling deformation depends on the prestrain of the actuation layer, the thickness ratio (t_a/t_p), and the thickness-to-length ratio (t_a/L). An analytic model is developed to capture the effect of these design parameters on the actuation deformations, which can explain quantitatively the experimental results in Fig. 1b.

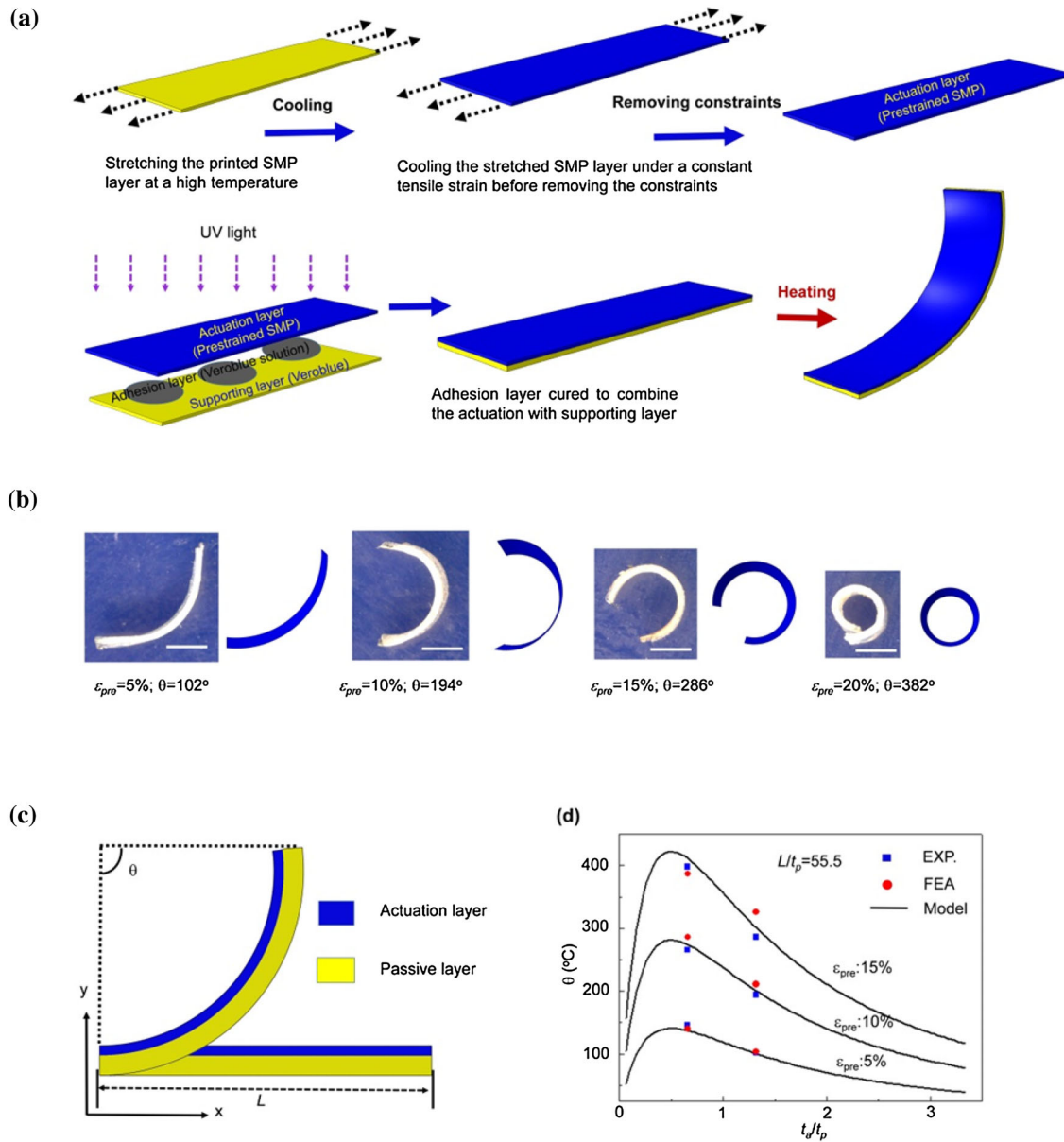


Fig. 1. Rolling deformation of a laminated SMP. **a** Schematic illustration of the fabrication procedure for the laminated SMP consisting of a prestrained layer. **b** Optical images and the corresponding FEA results for the rolled SMP strip by using different levels of prestrain ($\epsilon_{pre} = 5\%$, 10% , 15% , and 20%), fixed length (10 mm), and thickness of different layers ($60\ \mu\text{m}$, $30\ \mu\text{m}$, and $120\ \mu\text{m}$ for the actuation, adhesion, and supporting layers, respectively). **c** Schematic illustration of the mechanics model for the bilayer SMP structure. **d** Results of experiment, FEA, and model predictions on the rolling angle versus the thickness ratio (t_a/t_p) for three different prestrains ($\epsilon_{pre} = 5\%$, 10% , and 15%). The geometric parameters are fixed as $L/t_p = 55.5$. Scale bars, 3 mm

According to the Euler beam theory, the bilayer ribbon deforms into an arc shape for a uniformly prestretched actuation layer. The arc angle (θ) can then be adopted to characterize the degree of rolling deformation. The static equilibrium requires:

$$\int_{A_{actuation}} \sigma_{actuation} dA + \int_{A_{passive}} \sigma_{passive} dA = 0 \tag{1}$$

$$\int_{A_{actuation}} \sigma_{actuation} y dA + \int_{A_{passive}} \sigma_{passive} y dA = 0 \tag{2}$$

Here, σ and A represent the stresses and cross-sectional areas of different layers, and y is the distance from the neutral mechanical axis of the bilayer beam. For linear elastic constitutive relations, the stresses ($\sigma_{\text{actuation}}$ and σ_{passive}) in the actuation and passive layers are related to the strains ($\varepsilon_{\text{actuation}}$ and $\varepsilon_{\text{passive}}$) by:

$$\sigma_{\text{actuation}} = E_{\text{actuation}} (\varepsilon_{\text{actuation}} - \varepsilon_{\text{pre}}); \quad \sigma_{\text{passive}} = E_{\text{passive}} \varepsilon_{\text{passive}} \quad (3)$$

Here, the elastic moduli of the actuation and passive layers ($E_{\text{actuation}}$ and E_{passive}) are equal to E_{SMP} , the elastic modulus of SMP. For relatively small prestrains (e.g., $< 15\%$), it is reasonable to assume a negligible elongation in the arc length of the neutral mechanical axis, such that the strain in each layer can be given by:

$$\varepsilon_{\text{actuation}} = \varepsilon_{\text{pre}} + ky; \quad \varepsilon_{\text{passive}} = ky \quad (4)$$

where k is the curvature that can be determined by solving Eqs. (1)–(4), as given by

$$k = \frac{6\varepsilon_{\text{pre}}t_{\text{a}}t_{\text{p}}}{(t_{\text{a}} + t_{\text{p}})^3} \quad (5)$$

The arc angle of the rolled ribbon, i.e., the rolling angle (θ), can then be solved as

$$\theta = kL = \frac{6\varepsilon_{\text{pre}}(L/t_{\text{p}})(t_{\text{a}}/t_{\text{p}})}{(1 + t_{\text{a}}/t_{\text{p}})^3} \quad (6)$$

The analytic solution (Eq. (6)) agrees well with both the experimental and the FEA results for different prestrains and thickness ratios, as shown in Fig. 1d. Equation 6 also suggests a linear dependence of the rolling angle on the prestrain (ε_{pre}). As the thickness ratio increases, the rolling angle increases gradually to reach a peak value and then decreases, indicating the existence of an optimal thickness ratio to maximize the rolling angle. This is due to the competition between two different factors, i.e., the driving force of the actuation layer and the distance between the neutral mechanical plane of the laminated structure and the middle layer of the actuation layer. As the thickness ratio ($t_{\text{a}}/t_{\text{p}}$) increases, the former factor increases for a fixed thickness (t_{p}), while the latter decreases. The validated analytic model can serve as a reference for the design of reprogrammable 3D mesostructures, as discussed subsequently. In the FEA, the commercial software (ABAQUS) was used to capture all mechanics aspects of the global buckling and local rolling process. Four-node shell elements were used for the laminated 2D precursor, and eight-node solid elements were used for the elastomeric substrate. The refined meshes ensured computational accuracy. The elastic modulus and Poisson's ratio are 2 GPa and 0.40 for the SMP at room temperature (22 °C), 9.6 MPa and 0.40 for the SMP at a high temperature (100 °C), and 166 kPa and 0.49 for the substrate.

3. Reprogrammable 3D Mesostructures Based on Combined Global Buckling and Local Rolling

The thermally activated rolling deformations provide a viable route to reprogrammable 3D mesostructures, when combined with the mechanically guided assembly through compressive buckling. Based on the fabrication techniques described in Fig. 1, a patterned actuation layer (i.e., prestrained SMP) can be well laminated with a strategically designed passive layer (Veroblue) to form the 2D precursor structure. As shown in Fig. 2a, this 2D precursor structure was then transferred onto a prestretched elastomeric substrate that serves as the assembly platform. Only four anchors of the 2D precursor were strongly bonded with the prestretched platform, while other areas were simply weak interfaces. Release of the prestretch in the platform then drives the 2D-to-3D assembly through global buckling, leading to the formation of a deterministic 3D mesostructure. Upon exposure to a high temperature, the local rolling following from the shape recovery of the prestrained SMP enables the assembled 3D mesostructures to reshape into a different geometry.

Figure 2b summarizes four different reprogrammable mesostructures achieved using the above approach. In the 2D precursor designs, the prestrained SMP layers are integrated with printed passive layers on the top (dark blue) or bottom (light blue) side before the mechanically guided assembly. Here, the different types of placement (i.e., top and bottom sides) result in rolling deformations along different directions. The first three examples in Fig. 2b all experience an upward rolling at the actuation

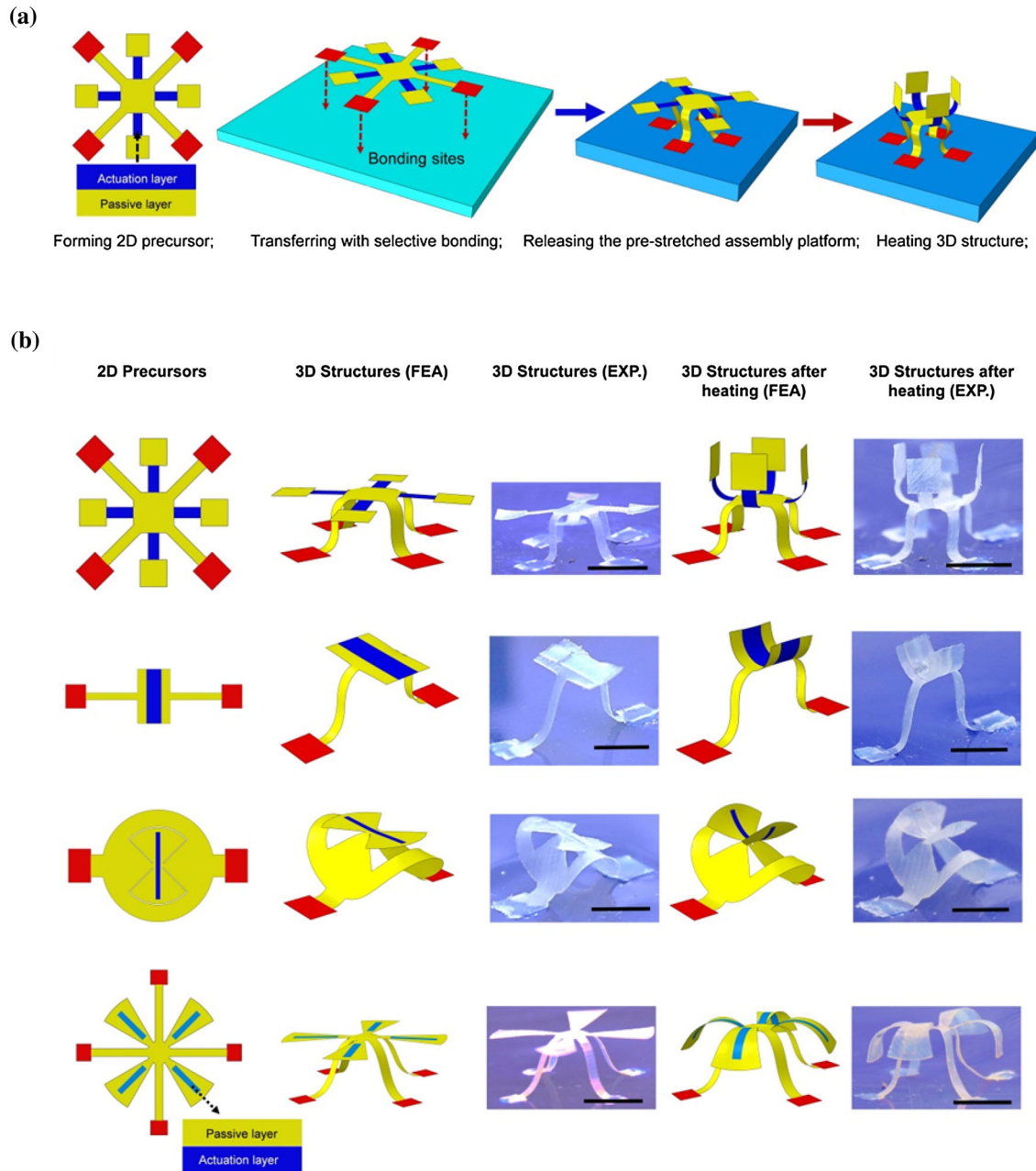


Fig. 2. Assembly procedure and various examples of reprogrammable 3D mesostructures. **a** Results of finite element analyses (FEA) that illustrate the assembly of reprogrammable 3D mesostructures through compressive buckling, which can be further reshaped through controlled local rolling. **b** 2D precursors, FEA predictions, and experimental images for five reprogrammable 3D mesostructures. The red regions of 2D precursors denote the parts bonded onto the substrate. The dark blue and light blue represent the areas that incorporate prestrained SMP on the top and bottom sides, respectively. Scale bars, 10 mm

regions, during the 3D reshaping. By contrast, the fourth example is transformed into a ‘coconut tree’ shape with four branches rolling downwards upon thermal activation. Unlike most of the examples reported previously [47, 53, 54], the final 3D configurations demonstrated here do not correspond to any of the buckling modes of the 2D precursors and thereby cannot be achieved directly through the compressive buckling.

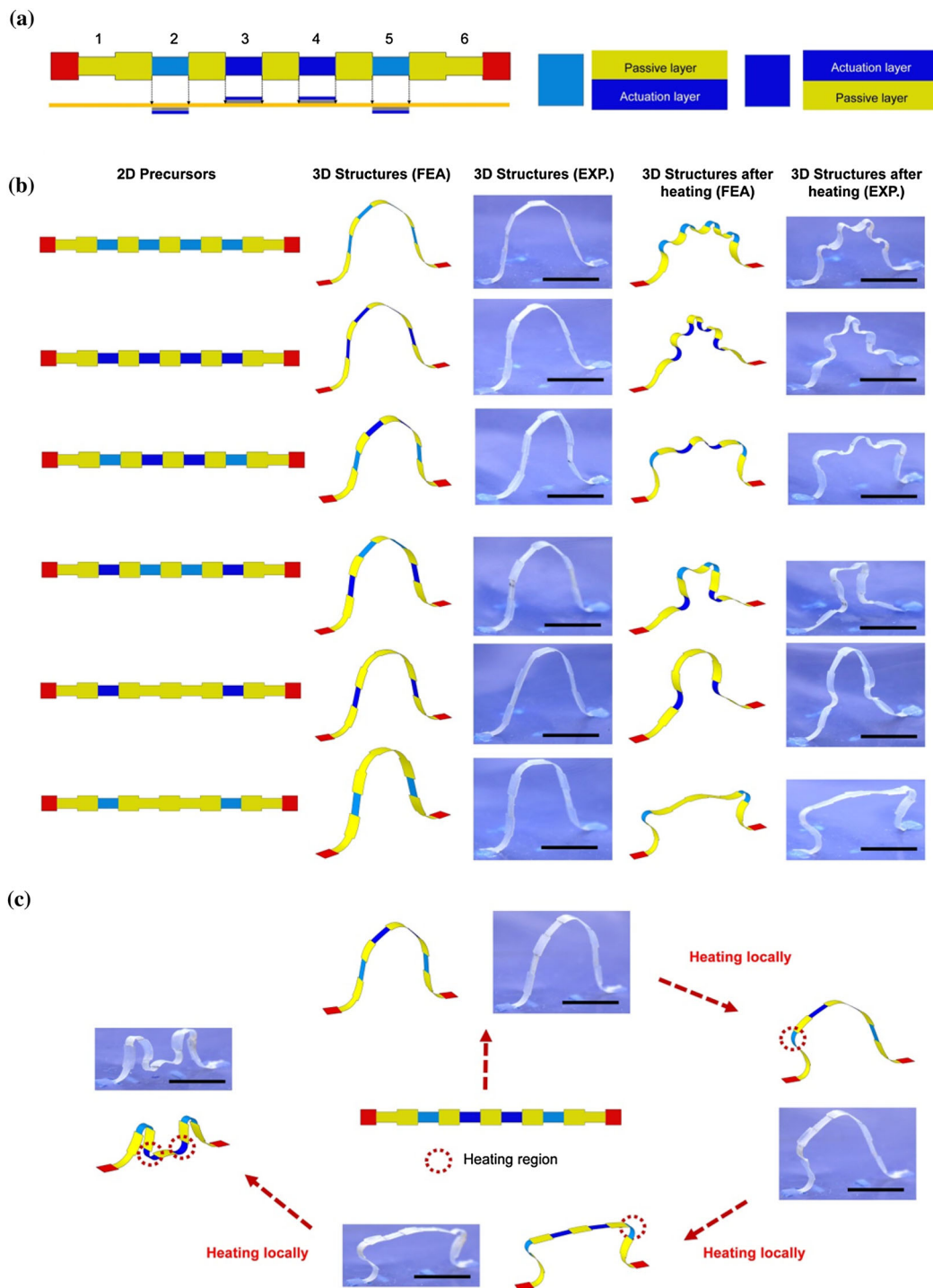


Fig. 3. Heterogeneous designs to achieve mesostructures whose configurations can be reprogrammed between diverse 3D shapes. **a** Illustration of a straight ribbon that consists of six narrow segments, either with or without addition of prestrained SMP layers. **b** 2D precursors, FEA predictions, and experimental images for the reprogrammable curvy ribbons formed from precursors with the same layout and different arrangements of actuation layers. **c** A 3D curvy ribbon that can be reshaped for multiple times, following a sequential, selective heating of different actuation segments. The dark blue and light blue represent the areas that incorporate prestrained SMP on the top and bottom sides, respectively. Scale bars, 10 mm

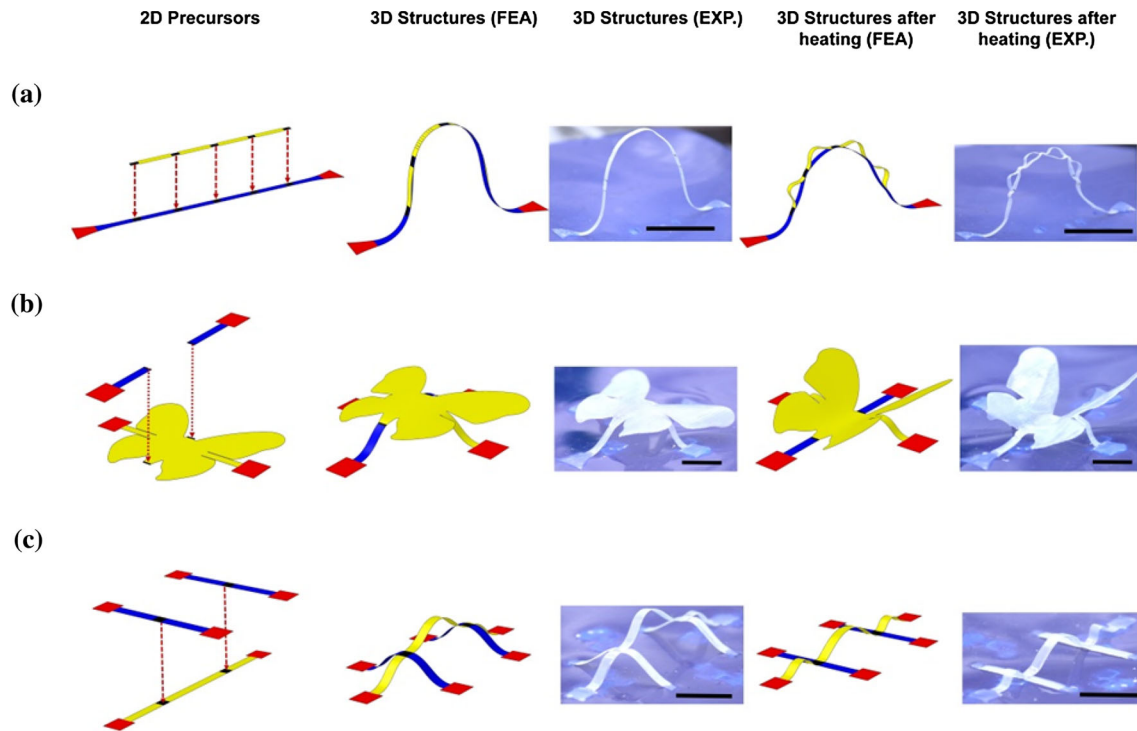


Fig. 4. Direct integration of prestrained SMP to reshape the mechanically assembled 3D mesostructures. **a** A hierarchically assembled curvy ribbon structure. **b** A butterfly undergoing a flapping motion upon exposure to a high temperature. **c** A wavy ribbon that can be reshaped from a large single wave into three small waves. Scale bars, 10 mm

According to the above discussions, both the location of prestrained SMP layer and the way (up or bottom) of placement onto the passive layer represent key parameters that affect the reshaping process of the assembled 3D mesostructure. Figure 3a presents a simple example in a straight ribbon consisting of six narrow segments either with or without integration with the actuation layers. In the condition with use of the actuation layer, both the topside and bottom-side placements were considered. Since many different combinations of the actuation-layer placement (i.e., top, bottom and no) can be exploited, a variety of final 3D configurations can be accessed, even when the 2D precursors have the same layout. Figure 3b provides six representative examples in this context, and their actuation-layer placements are illustrated in the leftmost column. Despite the different 2D precursor designs, the mechanically assembled 3D mesostructures do not exhibit a very clear difference in their geometries (see the second and third columns of Fig. 3b). However, upon exposure to a high temperature, the 3D arc mesostructures were reshaped into a number of distinct wavy configurations (see the two rightmost columns of Fig. 3b), indicating the powerful capability in 3D reconfiguration. Additionally, multiple mode switches can be realized when the prestrained SMP layer is heated individually (e.g., using a heating probe with 2 mm in diameter), as shown in Fig. 3c, where three new 3D configurations appear. It is noteworthy that although the 2D precursor design of Fig. 3c is exactly the same as the third example of Fig. 3b, the final 3D configuration is completely different, suggesting that the reshaping process also depends on the ‘heating path’ (i.e., the thermal loading path). In these experiments, ε_{pre} , t_{a} , and t_{p} are 10%, 60 μm , and 90 μm , respectively.

4. Reprogrammable 3D Mesostructures Based on the Direct Integration of Prestrained SMP

Since the SMP can store a relatively high level (e.g., $\sim 20\%$) of prestretch, the prestrained SMP layer can also reshape the 3D mesostructures through its direct shrinkage, without the need to laminate with any passive layers. Figure 4 provides three representative designs, as well as the experimental and

computational results. In the first example (Fig. 4a), a printed ribbon was selectively bonded onto a prestrained SMP ribbon (dark blue) to serve as the 2D precursor structure. The compressive buckling leads to the formation of a 3D arc structure. After experiencing a high temperature, the prestrained SMP ribbon tends to recover to its original shape, inducing shrinkage of this ribbon along the central axis. Such shrinkage results in a secondary compressive buckling in the top ribbon, thereby forming a hierarchical 3D ribbon structure (the two rightmost images of Fig. 4a). The biotical motion, such as the flap of the butterfly's wings, is also possible through the thermal activation of appropriately designed 2D precursors. Figure 4b presents an example, in which the recovery of two legs (i.e., prestrained SMP, dark blue) enables the central part of the 3D butterfly to move downwards and its wings to turn upwards. Figure 4c illustrates a design that reshapes a wavy ribbon from a large single wave into three small waves. In these experiments, ε_{pre} , t_a , and t_p are 20%, 120 μm , and 150 μm , respectively.

5. Conclusions

In summary, this manuscript presents a strategy to reshape the mechanically assembled 3D mesostructures, through the use of prestrained SMP layer in the 2D precursor design. An analytic model, as validated by both experiments and FEA, can capture well the effects of prestrain and thickness ratio on local rolling deformations. The proposed strategy enables the construction of 3D mesostructures with suspended curvy features or hierarchical geometries, through coordinated global buckling and local rolling deformations. Over a dozen of examples demonstrate the capability of the proposed strategy to achieve a diversity of reprogrammable 3D mesostructures, through the strategic selections of 2D precursor layouts, location of prestrained SMP layer, bonding conditions, and even heating paths. Additional opportunities may follow from the use of the proposed strategy in fabricating functional 3D reprogrammable devices.

Acknowledgements. X.G. and Z.X. contributed equally to this work. Y.Z. acknowledges the support from the National Natural Science Foundation of China (Grant Nos. 11502129 and 11722217) and the Tsinghua National Laboratory for Information Science and Technology. Y.H. acknowledges the support from the NSF (Grant Nos. CMMI1400169, CMMI1534120 and CMMI1635443). X.G. acknowledges the support from the National Natural Science Foundation of China (Grant Nos. 11702155).

References

- [1] Zhang H, Yu X, Braun PV. Three-dimensional bicontinuous ultrafast-charge and -discharge bulk battery electrodes. *Nat Nanotechnol.* 2011;6(5):277–81.
- [2] Wu H. Stable Li-ion battery anodes by in-situ polymerization of conducting hydrogel to conformally coat silicon nanoparticles. *Nat Commun.* 2013;4:1943.
- [3] Pikul JH. High-power lithium ion microbatteries from interdigitated three-dimensional bicontinuous nanoporous electrodes. *Nat Commun.* 2013;4:1732–6.
- [4] Sun K. 3D printing of interdigitated Li-ion microbattery architectures. *Adv Mater.* 2013;25(33):4539–43.
- [5] Wei TS. 3D printing of customized li-ion batteries with thick electrodes. *Adv Mater.* 2018;30(16):e1703027.
- [6] Dong K. 3D orthogonal woven triboelectric nanogenerator for effective biomechanical energy harvesting and as self-powered active motion sensors. *Adv Mater.* 2017;29(38):1702648.
- [7] Song Z. Origami lithium-ion batteries. *Nat Commun.* 2014;5:3140.
- [8] Song J, Feng X, Huang Y. Mechanics and thermal management of stretchable inorganic electronics. *Natl Sci Rev.* 2016;3(1):128–43.
- [9] Schaedler TA, et al. Ultralight metallic microlattices. *Science.* 2011;334(6058):962–5.
- [10] Soukoulis CM, Wegener M. Past achievements and future challenges in the development of three-dimensional photonic metamaterials. *Nat Photon.* 2011;5(9):523–30.
- [11] Zheng X, et al. Ultralight, ultrastiff mechanical metamaterials. *Science.* 2014;344(6190):1373–7.
- [12] Tian B. Macroporous nanowire nanoelectronic scaffolds for synthetic tissues. *Nat Mater.* 2012;11(11):986–94.
- [13] Mannoor MS. 3D printed bionic ears. *Nano Lett.* 2013;13(6):2634–9.
- [14] Leong TG. Tetherless thermobiochemically actuated microgrippers. *Proc Natl Acad Sci USA.* 2009;106(3):703–8.
- [15] Feiner R. Engineered hybrid cardiac patches with multifunctional electronics for online monitoring and regulation of tissue function. *Nat Mater.* 2016;15(6):679–85.
- [16] Liu X. 3D printing of living responsive materials and devices. *Adv Mater.* 2018;30(4):1704821.

- [17] Ahn BY. Omnidirectional printing of flexible, stretchable, and spanning silver microelectrodes. *Science*. 2009;323(5921):1590–3.
- [18] Huang W. On-chip inductors with self-rolled-up SiNx nanomembrane tubes: a novel design platform for extreme miniaturization. *Nano Lett.* 2012;12(12):6283–8.
- [19] Grimm D. Rolled-up nanomembranes as compact 3D architectures for field effect transistors and fluidic sensing applications. *Nano Lett.* 2013;13(1):213–8.
- [20] Zhang K. Origami silicon optoelectronics for hemispherical electronic eye systems. *Nat Commun.* 2017;8(1):1782.
- [21] Jang KI. Self-assembled three dimensional network designs for soft electronics. *Nat Commun.* 2017;8:15894.
- [22] Zheng ZG. Light-patterned crystallographic direction of a self-organized 3D soft photonic crystal. *Adv Mater.* 2017;29(42):1703165.
- [23] Guo SZ. 3D printed stretchable tactile sensors. *Adv Mater.* 2017;29(27):1701218.
- [24] Cho JH, et al. Nanoscale origami for 3D optics. *Small.* 2011;7(14):1943–8.
- [25] Liu Z. 3D-structured stretchable strain sensors for out-of-plane force detection. *Adv Mater.* 2018;30(26):1707285.
- [26] Chen Z, Chen W, Song J. Buckling of a stiff thin film on an elastic graded compliant substrate. *Proc Math Phys Eng Sci.* 2017;473(2208):20170410.
- [27] Yang H. 3D printed photoresponsive devices based on shape memory composites. *Adv Mater.* 2017;29(33):1701627.
- [28] Yuan C. 3D printed reversible shape changing soft actuators assisted by liquid crystal elastomers. *Soft Matter.* 2017;13(33):5558–68.
- [29] Compton BG, Lewis JA. 3D-printing of lightweight cellular composites. *Adv Mater.* 2014;26(34):5930–5.
- [30] Kolesky DB. 3D bioprinting of vascularized, heterogeneous cell-laden tissue constructs. *Adv Mater.* 2014;26(19):3124–30.
- [31] Zhu W. 3D-printed artificial microfish. *Adv Mater.* 2015;27:4411–7.
- [32] Cangialosi A, et al. DNA sequence-directed shape change of photopatterned hydrogels via high-degree swelling. *Science.* 2017;357:1126–30.
- [33] Zhang B. Reprocessable thermosets for sustainable three-dimensional printing. *Nat Commun.* 2018;9(1):1831.
- [34] Truby RL. Soft somatosensitive actuators via embedded 3D printing. *Adv Mater.* 2018;30(15):1706383.
- [35] Hsiao LC, et al. 3D printing of self-assembling thermoresponsive nanoemulsions into hierarchical mesostructured hydrogels. *Soft Matter.* 2017;13(5):921–9.
- [36] Huang Y, et al. Versatile, kinetically controlled, high precision electrohydrodynamic writing of micro/nanofibers. *Sci Rep.* 2014;4:5949.
- [37] Ye D. Large-scale direct-writing of aligned nanofibers for flexible electronics. *Small.* 2018;14(21):e1703521.
- [38] Py C. Capillary origami: spontaneous wrapping of a droplet with an elastic sheet. *Phys Rev Lett.* 2007;98(15):156103.
- [39] Yang Y. Solvent-assisted programming of flat polymer sheets into reconfigurable and self-healing 3D structures. *Nat Commun.* 2018;9(1):1906.
- [40] Hawkes E. Programmable matter by folding. *Proc Natl Acad Sci USA.* 2010;107(28):12441–5.
- [41] Mao Y. Programmable bidirectional folding of metallic thin films for 3D chiral optical antennas. *Adv Mater.* 2017;29(19):1606482.
- [42] Cui J, Adams JGM, Zhu Y. Pop-up assembly of 3D structures actuated by heat shrinkable polymers. *Smart Mater Struct.* 2017;26(12):125011.
- [43] Cui J, Adams JGM, Zhu Y. Controlled bending and folding of a bilayer structure consisting of a thin stiff film and a heat shrinkable polymer sheet. *Smart Mater Struct.* 2018;27(5):055009.
- [44] Lin SY, et al. A three-dimensional photonic crystal operating at infrared wavelengths. *Nature.* 1998;394:251–3.
- [45] Noda S. Full three-dimensional photonic bandgap crystals at near-infrared wavelengths. *Science.* 2000;289:604–6.
- [46] Qi M, et al. A three-dimensional optical photonic crystal with designed point defects. *Nature.* 2004;429:538–42.
- [47] Yan Z. Three-dimensional mesostructures as high-temperature growth templates, electronic cellular scaffolds, and self-propelled microrobots. *Proc Natl Acad Sci USA.* 2017;114(45):E9455–64.
- [48] Zhang Y. Printing, folding and assembly methods for forming 3D mesostructures in advanced materials. *Nat Rev Mater.* 2017;2:17019.
- [49] Rogers J. Origami MEMS and NEMS. *Mrs Bull.* 2016;41(2):123–9.

- [50] Xu S, et al. Assemble of micro/nanomaterials into complex, three-dimensional architectures by compressive buckling. *Science*. 2015;347(6218):154–9.
- [51] Fan Z, et al. A double perturbation method of postbuckling analysis in 2D curved beams for assembly of 3D ribbon-shaped structures. *J Mech Phys Solids*. 2018;111:215–38.
- [52] Fu H. Morphable 3D mesostructures and microelectronic devices by multistable buckling mechanics. *Nat Mater*. 2018;17:268–76.
- [53] Yan Z, et al. Controlled mechanical buckling for origami-inspired construction of 3D microstructures in advanced materials. *Adv Funct Mater*. 2016;26(16):2629–39.
- [54] Zhang Y. A mechanically driven form of Kirigami as a route to 3D mesostructures in micro/nanomembranes. *Proc Natl Acad Sci USA*. 2015;112(38):11757–64.